ADVANCED MATERIALS
www.advmat.de

Interstitial Segregation has the Potential to Mitigate Liquid Metal Embrittlement in Iron

Ali Ahmadian, Daniel Scheiber, Xuyang Zhou, Baptiste Gault, Lorenz Romaner,* Reza D. Kamachali, Werner Ecker, Gerhard Dehm,* and Christian H. Liebscher**

The embrittlement of metallic alloys by liquid metals leads to catastrophic material failure and severely impacts their structural integrity. The weakening of grain boundaries (GBs) by the ingress of liquid metal and preceding segregation in the solid are thought to promote early fracture. However, the potential of balancing between the segregation of cohesion-enhancing interstitial solutes and embrittling elements inducing GB de-cohesion is not understood. Here, the mechanisms of how boron segregation mitigates the detrimental effects of the prime embrittler, zinc, in a Σ5 [001] tilt GB in α-Fe (4 at.% Al) is unveiled. Zinc forms nanoscale segregation patterns inducing structurally and compositionally complex GB states. Ab initio simulations reveal that boron hinders zinc segregation and compensates for the zinc-induced loss in GB cohesion. The work sheds new light on how interstitial solutes intimately modify GBs, thereby opening pathways to use them as dopants for preventing disastrous material failure.

1. Introduction

Grain boundary (GB) properties such as cohesive strength or mobility can be significantly altered through segregation of alloying elements or impurities.[1] One of the most detrimental elements impacting the properties of GBs in iron (Fe) and steel is zinc (Zn), which promotes brittle intergranular fracture of the material through liquid metal induced embrittlement (LMIE).[2–9]

Several models were proposed to explain the underlying mechanisms leading to LMIE.[10] The Stoloff–Johnson–Westwood–Kamdar (SJWK) model considers that the liquid metal adsorbed at the crack tip promotes crack propagation under an applied stress by weakening the strength of the interatomic bonds.[11,12] In contrast, stress-assisted GB diffusion preceding the crack initiation is assumed to be the root cause for the increase in GB brittleness in the Krishtal–Gordon–An model.[13] DiGiovanni et al.[14] investigated the diffusion of Zn in Fe by means of electron-probe microanalysis (EPMA) before and after mechanical loading. Their observations confirmed that stress-assisted diffusion in the vicinity of the crack tip is one of the dominant mechanisms. There are various explanations on the origin of the segregation induced GB embrittlement process. Atomic size differences in Cu–Bi, also an LMIE system, were shown to cause local strain fields, which facilitate a reduction in GB cohesion.[15] However, the size differences between Fe and Zn are not large enough to play a major role. Instead electronic effects such as bonding type[16] and mobility[17–19] can be made responsible for GB embrittlement. Peng et al.[20] performed first-principles tensile tests on a Zn segregated Σ5 [001] GB in ferritic Fe. They found a weakening of the GB because of covalent bonding between Zn and Fe, which ultimately reduces the charge density between the Fe atoms and hence their bond strength.

In order to prevent LMIE, it was proposed to introduce cohesion enhancing alloying elements to GBs. Scheiber et al.[9] concluded from ab initio and thermodynamic modeling that the embrittling effect of Zn at different symmetrical body-centered-cubic (bcc)-Fe tilt GBs can be reduced by Al and Si, which is related to site-competition as well as repulsive interactions between the solutes and Zn. Although a large body of experimental and theoretical studies on LMIE exist,[21–23] a fundamental understanding on the relationships between the GB structure, Zn

A. Ahmadian[+], X. Zhou, B. Gault, G. Dehm, C. H. Liebscher
Max-Planck-Institut fuer Eisenforschung GmbH
40237 Düsseldorf, Germany
E-mail: a.ahmadian@mpie.de; dehm@mpie.de; liebscher@mpie.de

D. Scheiber, L. Romaner, W. Ecker
Materials Center Leoben GmbH
Leoben 8700, Austria

B. Gault
Department of Materials, Royal School of Mines
Imperial College London
London UK

L. Romaner
Montanuniversität Leoben
Leoben 8700, Austria
E-mail: lorenz.romaner@unileoben.ac.at

R. D. Kamachali
Federal Institute for Materials Research and Testing (BAM)
Unter den Eichen 87
12205 Berlin, Germany

The ORCID identification number(s) for the author(s) of this article can be found under https://doi.org/10.1002/adma.202211796

[+]Present address: Institute of Nanotechnology, Karlsruhe Institute of Technology, 76344 Eggenstein-Leopoldshafen, Germany

DOI: 10.1002/adma.202211796

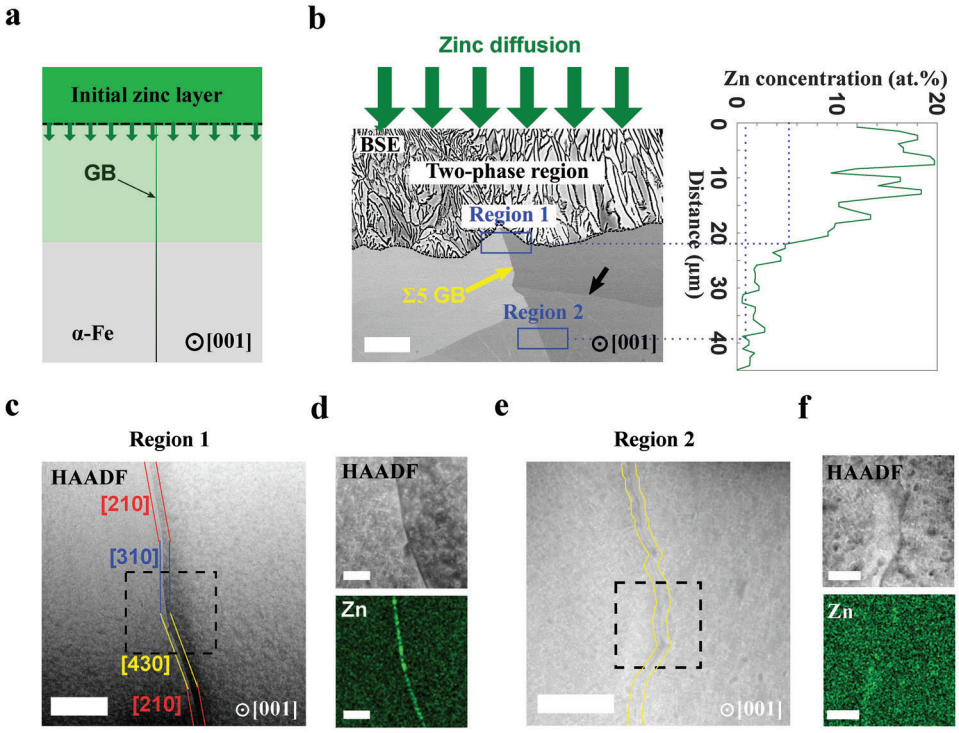

Figure 1. Overview BSE images of the Σ5 [001] GB. a,b) The diffusion of Zn results in the formation of a two-phase region containing α-Fe and Γ-Fe–Zn phases. STEM specimen were extracted from two regions (indicated by blue rectangles). b) Region 1 marks an area of the GB in the vicinity of the two-phase region, while Region 2 is ≈40 μm away from the two-phase region. Furthermore, (b) shows a low-angle GB (indicated by a black arrow) intersecting with the Σ5 GB and locally bending it. c,d) Region 1: c) HAADF-STEM image of the Σ5 GB viewed along the [001] tilt axis. The GB is inclined and the boundary plane can be divided into nearly symmetric (210), (430), and (310) segments. d) STEM–EDS mapping of the region, which is indicated in (c) by a black dashed rectangle. The GB is enriched by Zn with a weak decrease from top to bottom. e,f) Region 2: e) HAADF-STEM image shows strong inclinations of the boundary. f) Corresponding STEM–EDS map of the black dashed rectangle region shows no clear enrichment of Zn. Scale bar in (b): 10 μm; in (c): 100 nm; in (d),:20 nm; in (e): 50 nm; and in (f): 20 nm.

segregation and its impact on embrittlement is lacking. Especially, the role of interstitial solutes on the embrittlement of GBs by Zn has not been considered, while, for example, C and B are known to act as GB cohesion enhancers in Fe-based alloys.[24–29] Miyazawa et al.[28] have shown by first-principles based calculations that segregation of C would increase the GB cohesion in Fe. In contrast to C, B can occupy substitutional as well as interstitial positions in α-Fe[30] and would enhance the cohesion strength of the GB when taking up interstitial positions.[18] Therefore, it is of great interest to understand how cohesion enhancing solutes such as B and C impact the segregation behavior of Zn and how their interplay affects the detrimental effect of Zn on GB cohesion on an atomistic level.

Here, we study the local atomic structure and composition of a Σ5 (310)[001] tilt GB in a bicrystal of bcc Fe at different levels of Zn segregation. By atomically resolved microscopic probing techniques, we find that Zn forms nanometer sized segregation lines in a region preceding the former solid–liquid interface. However, both B and C are homogeneously distributed across the GB plane. The Zn-segregation pattern formation is explained by density-based phase-field simulations revealing a miscibility gap of the GB, which promotes a GB phase decomposition. Furthermore, our ab initio calculations show that the presence of B and C significantly reduces the segregation energy of Zn due to strong repulsive interactions, which also leads to a reduction of the maximum Zn concentration at the GB. Interestingly, B is capable to compensate for the reduction in the work of separation through Zn even for high Zn GB concentrations. Our work suggests that interstitial solutes such as B and C have the potential to mitigate the embrittling tendency of Zn. These insights provide pathways to prevent liquid metal embrittlement in Fe by controlled addition of cohesion enhancing elements.

2. Results

2.1. Global Grain Boundary Structure

We use a bicrystal containing a Σ5 (310)[001] tilt GB with trace amounts of B and C to study Zn segregation from the liquid state into the GB and the interaction of Zn with the interstitial solutes. We formed a diffusion couple of Zn and the bicrystal, and subsequently annealed it at 800 °C to liquefy the Zn reservoir and enable diffusion of Zn into the solid Fe bicrystal as schematically shown in **Figure 1**a. The detailed experimental procedure is described in Experimental Section and Supporting Information. The backscattered electron (BSE) scanning electron microscopy (SEM) image in Figure 1b shows a two-phase region in the top part of the diffusion couple and a distinct interface between this region and the Fe bicrystal. Different Fe–Zn-type intermetallic phases are observed to form for up to ≈150 μm from

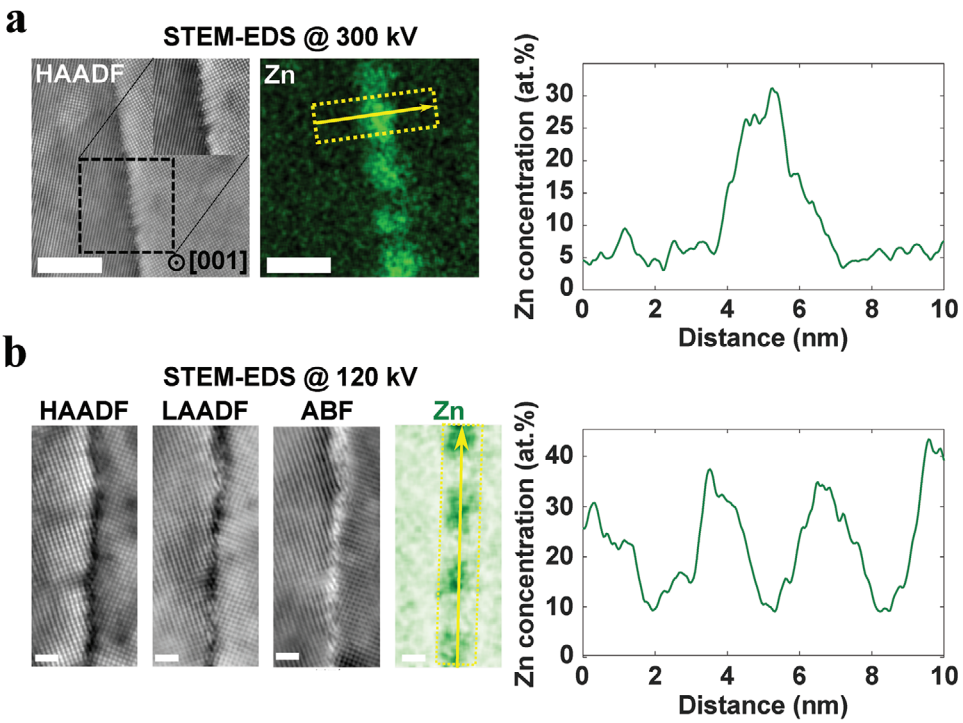

Figure 2. High-resolution STEM–EDS at different acceleration voltages. a) The HAADF-STEM and corresponding Zn elemental map show formation of Zn clusters with concentrations of ≈30 at.%. To improve the STEM–EDS resolution, the acceleration voltage was reduced to 120 kV as shown in (b). The incident electrons are scattered to lower angles due to the presence of the Zn clusters resulting in a dark contrast in the HAADF- as well as low-angle angular dark-field (LAADF)-STEM image but a bright contrast in the ABF-STEM image. The Zn concentration profile along the GB shows a periodicity of 3–4 nm with concentrations varying from 10 at.% to 40 at.%. Scale bar in (a): 5 nm; and in (b): 1 nm.

the top within the α-Fe matrix (see Figure 1b). In Figure S2 (Supporting Information), it is shown that a thick Zn-rich layer with ≥60 at.% Zn, corresponding to the Γ-Fe–Zn phase, is present at the GB in the two-phase region. Here, we limit our observations to the GB region below this two-phase region, where no intermetallic compounds formed in the bulk or at the GB. We specifically focus on two different GB areas indicated as "Region 1", which is Zn-rich with an average concentration of Zn determined by energy-dispersive X-ray spectroscopy (EDS) in the SEM of ≈5 at.%, and "Region 2" with an average Zn content of ≈0.5 at.% (see Figure 1b). Region 1 is ≈5 µm below the two-phase region and high-angle annular dark-field (HAADF) imaging along the [001] tilt axis in the scanning transmission electron microscopy (STEM) reveals that the GB inclination is locally deviating from the exact (310) habit plane (see Figure 1c). Corresponding STEM–EDS measurements shown in Figure 1d demonstrate strong segregation of Zn to the GB and suggest that it is inhomogeneously distributed along the GB. The GB in Region 2, which is ≈40 µm away from the two-phase region, is curved and exhibits a high density of local kinks as shown in Figure 1e. Zinc is only slightly enriched at the GB as shown in the elemental map in Figure 1f.

2.1.1. Near-Atomic-Scale Zinc Segregation

We performed near-atomic-resolution STEM–EDS elemental mapping in the Zn-rich Region 1 of the bicrystal. **Figure 2** shows atomic-resolution STEM images and the associated Zn distribution along the GB at acceleration voltages of 300 kV and 120 kV, respectively. The HAADF-STEM images in Figure 2a,b reveal that the GB structure appears disrupted by a high density of GB defects. Measurements at 120 kV shown in Figure 2b clearly demonstrate clustering of Zn at the GB into Zn-rich (≈35 at.%) and Zn-lean (≈10 at.%) regions having a width of ≈1 nm and a regular spacing of ≈3–4 nm. Although Zn has a slightly higher atomic number than Fe ($\Delta Z = 4$), the corresponding HAADF-STEM images do not show any indication of regions with higher intensity. More information on the STEM–EDS measurements will be discussed later.

To obtain further insights into the 3D arrangement of the Zn segregation and its correlation to the distribution of the impurity elements B and C, we performed atom probe tomography (APT) experiments from the same regions as our STEM investigations.

2.1.2. Grain Boundary Composition

Figure 3a presents the reconstructed 3D-volume of the needle-shaped specimen viewed along the [001] tilt axis extracted from Region 1 (Zn-rich), where the GB is positioned at a 45° angle ≈100 nm away from the apex. Besides the segregation of Zn, B and C are also observed to segregate to the GB. The 3D atom map of B shows a rather unusual behavior in the form of a tail that extends into the lower grain for nearly 50 nm, although it has been recognized that anomalies in the field evaporation of solutes can lead to asymmetric solute distribution at GBs.[31]

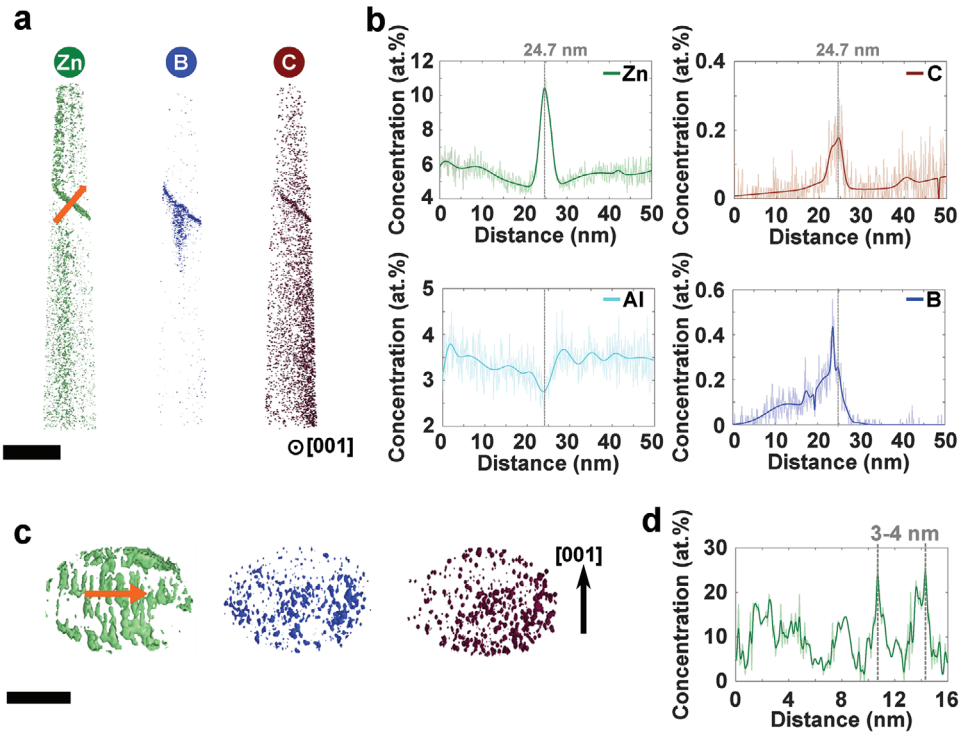

Figure 3. Segregation of Zn, B, C, and depletion of Al at the Σ5 [001] GB of Region 1. a) 3D APT reconstruction showing the distribution of Zn, B, and C viewed along the [001] tilt axis. Using an isoconcentration value of 10 at.% for Zn, 0.5 at.% for B and 0.3 at.% for C highlights the segregation of these elements to the GB. b) The composition profile extracted from a cylindrical region with diameter of 30 nm is extracted across the GB (shown in (a) as orange arrow). A clear increase of Zn, B, and C is shown at the GB, while the concentration of Al decreases. The maximum concentration peak of Zn and C is at 24.7 nm, while B concentration reaches the maximum already at 23.5 nm, the same as the minimum of Al. The Zn concentration first decreases slightly at the vicinity of the boundary until it increases steeply. The C and B concentration do not show such decrease at the vicinity of the GB. The B concentration shows a continuous increase over a large range of several tens of nanometers before reaching the maximum value and then it decreases abruptly to nearly 0 at.%. c) Rotation of the APT reconstruction in (a) such that the distribution of Zn, B and C onto the GB plane is shown, that is, the viewing direction is along the GB plane. While B and C show no formation of patches, Zn forms columnar patches elongated along the tilt axis. d) A concentration profile extracted along the orange arrow in (c) shows the concentration and distances of Zn columns. Scale bar in (a): 50 nm; and in (c): 20 nm.

The concentration profile of B extracted across the GB in Figure 3b verifies this observation, which will be discussed later. The bulk Zn concentration of ≈5.5 at.% from APT agrees with STEM–EDS measurements (Figure 2). The averaged GB concentration of Zn reaches a value of ≈10 at.%. As we have seen before, the Al concentration decreases to ≈2.7 at.% at the GB due to the presence of B and C.[24] Both concentration profiles of B and C show a broadened and asymmetric shape with a tail toward the left side corresponding to the lower grain in the reconstruction (Figure 3a). The peak concentration of B and C in the initially investigated GB before Zn segregation was 1.8 at.% and 2.4 at.%,[24] which is reduced by a factor of ≈4 and ≈10, respectively. A close inspection of the peak locations of the concentration profiles reveals an offset of the B peak of ≈1 nm with respect to that of the Zn concentration peak. A similar behavior was obtained in a different APT specimen as shown in Figure S6 (Supporting Information).

Observations of the in-plane distribution of Zn within the GB obtained by APT reveals that Zn is arranged in the form of segregation lines which are aligned along the [001] tilt axis (see Figure 3c,d). However, B and C show a homogeneous distribution within the GB plane as shown in Figure 3c. A similar modulation in Zn concentration was observed by STEM–EDS shown in Figure 2.

APT investigations were also performed in Region 2 (see Figure S5, Supporting Information), revealing a lower average bulk Zn content of ≈0.5 at.%. Interestingly, no clear indication for Zn segregation to the GB containing B and C with peak concentration values of ≈1.8 at.% and ≈0.8 at.%, respectively (shown in Figure S5b, Supporting Information), is found. In comparison to the Zn-rich Region 1 of Figure 3b, the peak B and C concentration at the GB in the Zn-lean Region 2 is nearly a factor of 4 higher, similar to values obtained in the as-grown bicrystal.[24] Furthermore, the concentration profiles of B and C adopt a symmetric shape, in contrast to that observed in Region 1 (Figure 3b).

2.1.3. Atomic Grain Boundary Structure

To explore the underlying atomic GB structure in both Region 1 (Zn-rich) and 2 (Zn-lean), we used atomic-resolution HAADF-STEM imaging as shown in **Figure 4**. The HAADF-STEM overview image of the GB in Region 1 shown in Figure S4a

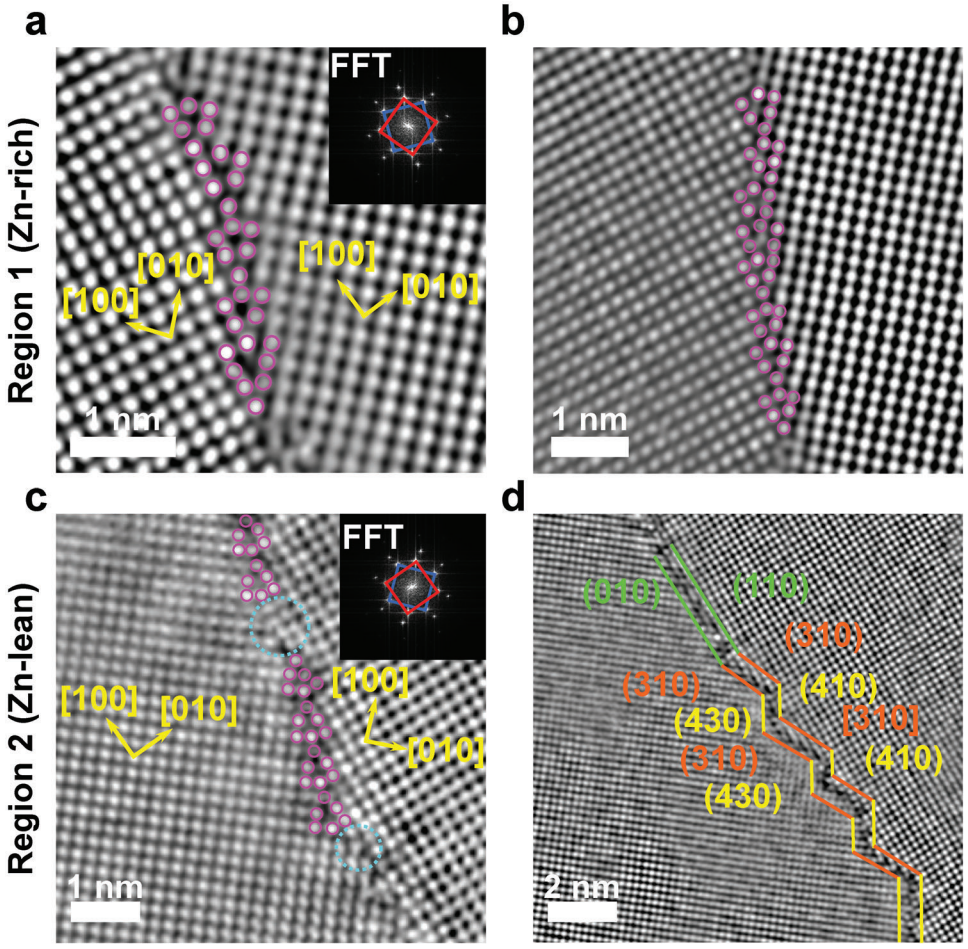

Figure 4. Atomic structure of the Σ5 [001] GB in the Fe-4at.%Al bicrystal. a,b) High-resolution HAADF-STEM images from Region 1 (Zn-rich) shows the formation of kite-type structural units (purple color), where extra atoms are introduced to shift the SU parallel and perpendicular to the boundary plane normal. From the FFT in (a) the misorientation angle is determined as 40°. c) High-resolution HAADF-STEM images from Region 2 (Zn-lean) of the area marked by the upper dashed square in Figure S4b (Supporting Information). The GB consists of perfect kite-type SU interrupted by GB defects, which result in the inclination of the boundary. d) High-resolution HAADF-STEM image of the region marked by the lower dashed square in Figure S4b, Supporting Information. The GB is faceting into symmetric (310)/(310) and asymmetric (430)/(410). Scale bar in (a–c): 1 nm; in (d): 2 nm.

(Supporting Information) reveals a slight curvature of the GB, which leads to the formation of different nanoscale GB facets with varying GB planes close to (310). The atomic-resolution images of Figure 4a,b shows that the GB structure is composed of kite-type structural units, which are disrupted by GB defects. Locally, the GB habit plane is varying between (310)- and (210)-type as well as asymmetric GB segments. It should be mentioned that we did not find any indication for the formation of intermetallic compounds, borides or carbides at the GB by high resolution STEM and STEM–EDS despite of the high peak concentration of Zn with more than 30 at.%, which would locally affect GB cohesion

The GB in Region 2 (Zn-lean) is composed of nanofacets with different GB plane inclinations (see Figure 1e; Figure S4b, Supporting Information). Figure S4b (Supporting Information) shows a magnified HAADF-STEM image of the GB in Region 2, where the GB alternates between symmetric (210) and asymmetric segments. The atomic GB structure in Figure 4c shows a near (310) GB with kite-type structural units, which are interrupted by GB steps or disconnections (highlighted by dashed cyan circles) to compensate for deviations in GB inclination. In other areas, in Region 2 the GB is dissociating into a nanofaceted structure (see Figure 4d).

2.1.4. Grain Boundary Decomposition

A comparison of the atomic structure of the GB in Region 1 with the nanoscale segregation pattern of Zn shows no direct explanation for the formation of Zn-rich clusters. Furthermore, there is no indication that Zn is preferentially segregating to GB defects. From a thermodynamic point of view, GBs can undergo structural transitions or decompose into regions with different solute excess upon segregation.[32]

In order to explore the nanoscale phase decomposition behavior of Zn at the Σ5 [001] (310) GB in dependence of the bulk Zn concentration, we used density-based thermodynamic and phase-field (DPF) modeling. The computational details are given in the

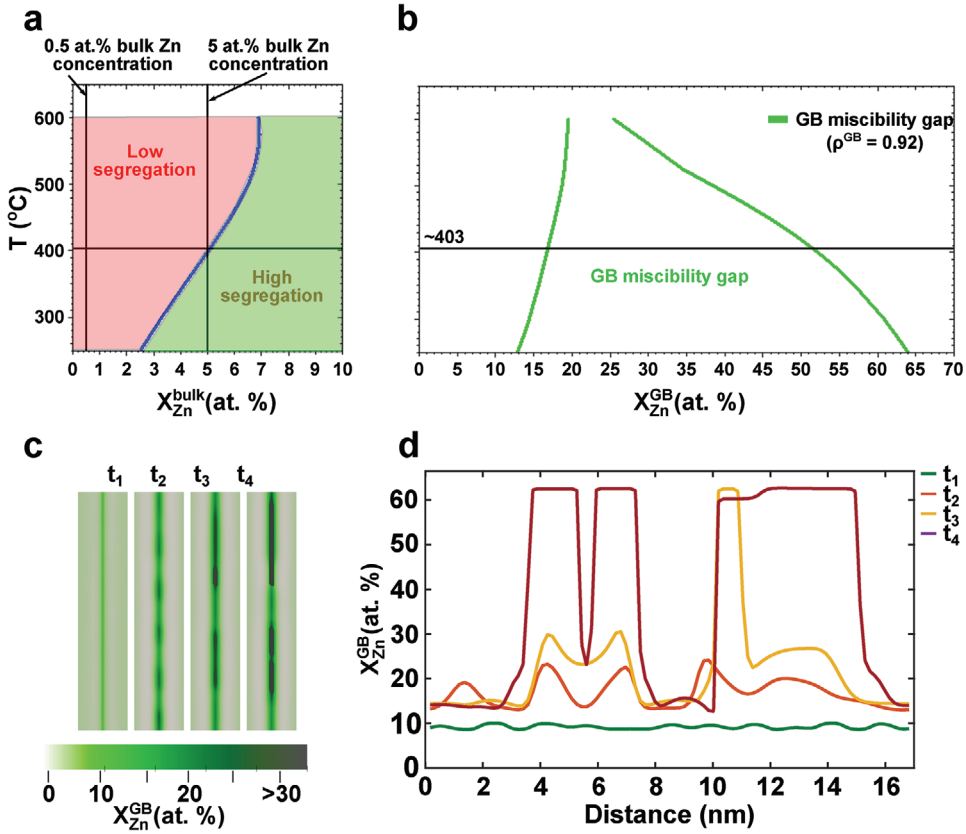

Figure 5. Density-based thermodynamic and phase-field simulation of 5 GB. a) Temperature and bulk Zn concentration dependence for which low and high Zn GB segregation occur, separated by the transition curve (blue line). For 0.5 at.% bulk Zn concentration, only low Zn GB segregation is observed, while for 5 at.% bulk Zn concentration, the GB would decompose into Zn-rich and Zn-lean regions according to the GB miscibility shown in (b). The critical temperature here for this transition from low to high Zn segregation is 403 °C. b) GB miscibility gap, when high Zn segregation occurs (green region in (a)). At a temperature of ≈403 °C and a bulk concentration of 5 at.%, the GB will show a phase decomposition with Zn concentrations of ≈17 at.% and ≈52 at.%. c) Edge-on view of the time evolution of the GB phase decomposition for a bulk Zn concentration of 5 at.% at 300 °C obtained by DPF simulations. The GB is oriented vertically. d) GB concentration profiles of Zn extracted from (c) for each time step t_i.

Experimental Section. In a first step, we modeled the GB phase diagram in the Fe–Zn system. The GB miscibility gap shown in **Figure 5**b is obtained for a GB density of 0.92, which corresponds to the Σ5 [001] GB studied here experimentally. Figure 5a shows the temperature dependence of the critical bulk Zn concentration for which a low and high Zn segregation tendency to the GB occurs. These regions are separated by the transition curve (blue line in Figure 5a. For low bulk concentrations of 0.5 at.%, such as found experimentally in Region 2, low segregation would occur but without any phase decomposition at the GB. The situation changes for a bulk concentration of 5 at.% (such as in Region 1). At a temperature of ≈403 °C, a bulk Zn concentration of 5 at.% is sufficient to promote high Zn GB segregation, which leads to a phase decomposition of the GB in regions with Zn concentration of ≈17 at.% and ≈57 at.% according to the GB phase diagram shown in Figure 5b. This temperature is highlighted by the black vertical line in Figure 5a,b. Our results reveal that the GB exhibits a miscibility gap comparable to the Fe–Zn bulk phase diagram (see Figure S8, Supporting Information). The origin of this phase separation in the α-Fe–Zn system is related to magnetic ordering.[33] Due to the existence of this miscibility gap, the GB can undergo a phase decomposition upon Zn segregation. This is dictated by the bulk alloy Zn concentration and temperature as determined by the equilibrium chemical potential.

With decreasing temperature, the Zn-rich domains further enrich in Zn up to ≈64 at.% (at 275 °C) and the concentration of the Zn-lean regions reduces slightly to ≈12 at.%. The time dependent GB phase evolution was investigated by 3D DPF simulations at 300 °C and a bulk Zn concentration of 5 at.% as shown in Figure 5c,d. Figure 5c shows the evolution of the Zn concentration in an edge on view at the GB for four different time steps. The in-plane evolution of the Zn-rich and Zn-lean domains are shown in Figure S10, Supporting Information. Initially, Zn is homogeneously distributed along the GB with a concentration of ≈9 at.%, as also seen in the concentration profiles extracted along the GB shown in Figure 5c (green curve). With progressing time, the GB phase separates into Zn-rich (≈60 at.%) and Zn-lean (≈17 at.%) domains, which are separated by ≈5 nm, consistent with the experimental observations. For a bulk Zn concentration of 0.5 at.%, no GB decomposition is observed according to the DPF simulations.

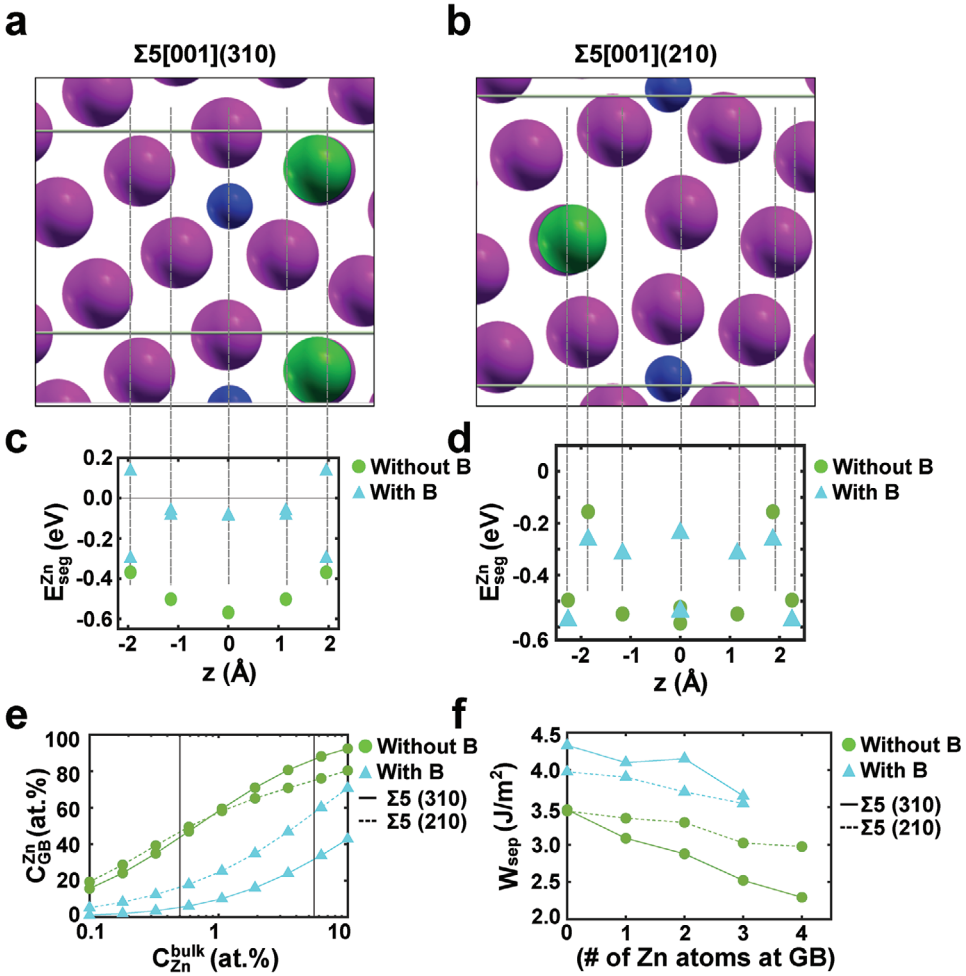

Figure 6. Modeling of Zn segregation to Σ5 [001] GB with and without B. a,b) Atomic structure of Σ5 [001](310) (a) and Σ5 [001](210) (b) GB with interstitial B (blue) and substitutional positions (purple = Fe, green = Zn). c,d) Zn segregation energies from DFT for Zn to pure GB (green circles) and to GB when B is present (cyan triangles). e) Zn concentration at the GB as a function of the Zn bulk concentration modeled for Σ5 [001](310) (solid line) as well as Σ5 [001](210) (dashed line) GB. For both GBs the enrichment level was calculated with (cyan) and without (green) B. The vertical lines highlight the observed Zn concentrations in the bulk—namely 0.5 at.% and 5.5 at.%. f) Modeled GB cohesion for different number of Zn atoms at Σ5 [001](310) (solid line) and Σ5 [001](210) (dashed line) GB with (cyan) B and for GBs where B is not present (green).

The predicted composition of the Zn-rich GB regions is higher than determined experimentally, since the GB phase decomposition is kinetically limited at lower temperatures in the experiment. This is evident from the APT measurements shown in Figure 3b, where depletion of Zn adjacent to the GB is indicating incomplete segregation due to limited diffusivity during the cooling process. Furthermore, the presence of B and C atoms at the GB may impact the segregation behavior of Zn to the GB and ultimately affect the Zn GB concentration.

2.1.5. Co-Segregation Behavior of Zn and B

In order to explore the interaction of B and C with Zn and their impact on the segregation behavior and GB cohesion, we performed first principles DFT calculations of the Σ5 (310) (see **Figure 6**a; Figure S7, Supporting Information) as well as Σ5 (210) (see Figure 6b) GBs. The effect of C on the Zn segregation behavior is similar to that of B as shown in Figure S7 (Supporting Information). From our previous ab initio and thermodynamic modeling studies, we observed that Al and Zn show a weak repulsive interaction behavior in a Σ5 Fe GB, with interaction energies of up to 0.05 eV, which is nearly one order of magnitude lower than that of B and Zn, respectively. Therefore, the effect of Al is considered to be negligible. Details on the computational approach can be found in the Experimental Section. The GB structures with all possible segregation sites considered for Zn (green) and B (blue) atoms are displayed in Figure 6a,b. The same calculations performed for C (brown) are shown in Figure S7 (Supporting Information). The segregation energies of Zn E^{Zn}_{seg} with and without interstitial B for the Σ5 (310) and (210) GBs are shown in Figure 6c,d. Zinc alone has a similarly high segregation energy for its lowest energy position at the GB center ($z = 0$ Å) in a substitutional site within the GB plane for both GBs of −0.57 and −0.58 eV, respectively. However, if B is present, the overall segregation energies of Zn are strongly reduced (see the cyan

triangles). Note that multiple possible configurations were investigated. For example, the presence of B lowers the segregation energy of Zn at the GB center position by a factor of ≈6 to −0.09 eV for the Σ5 (310) GB. Only for Zn farthest away from the GB considered here at $z = \pm 2$ Å, a slightly higher E_{seg}^{Zn} of −0.30 eV is obtained for a single configuration. A similar trend is observed for the Σ5 (210) GB, where the segregation energies are reduced by a factor of ≈2–3 in the presence of B. A possible configuration with Zn at the GB center with nearly the same segregation energy as without B is found. This suggests that the Σ5 (210) GB shows a slightly higher probability for Zn to segregate with B being present than the Σ5 (310) GB.

Based on the calculated segregation energies, we estimate the enrichment of Zn at the GB at 800 °C using the White–Coghlan isotherm [34] considering segregation to all sites at the GB. This allows us to explore the influence of the bulk Zn concentration and the impact of B on the expected amount of Zn at the GB in the theoretical high temperature limit, which corresponds to the annealing temperature of the bicrystal diffusion couple. Since both the Σ5 (310) and Σ5 (210) GBs show a similar minimum segregation energy of Zn alone, the Zn concentration is predicted to be nearly the same at both GBs. It increases monotonically with increasing Zn bulk content as shown in Figure 6e (green dots). When B is also present at the GBs, a strong reduction of the maximum Zn content can be observed for both interfaces. For the Σ5 (310) GB (solid lines) a reduction in the Zn concentration from 85 at.% to 30 at.% is observed for a bulk Zn concentration of 5.5 at.%, which corresponds to the Zn-rich Region 1 in the experiments. A similar trend is observed for lower Zn bulk contents. The reduction in GB Zn concentration is less pronounced for the Σ5 (210) boundary as illustrated in Figure 6e (dashed lines). These predictions indicate that B does not only strongly reduce the segregation energies, but with this also significantly lowers the maximum attainable Zn content at the GBs within the thermodynamic limit at the annealing temperature.

2.1.6. Grain Boundary Cohesion

To assess the effects of co-segregation of Zn and B on GB cohesion, we calculated the theoretical work of separation W_{sep} for the Σ5 (310) and Σ5 (210) GBs as shown in Figure 6f. GB cohesive properties were computed for each Zn concentration in the most preferential segregation state. Both GBs show very similar cohesive properties in the pure state without any solutes present resulting in a work of separation of 3.5 J m^{-2}. With the addition of a single B atom, corresponding to half a monolayer (ML) or ≈9 at.% and ≈6 at.% for the Σ5 (310) and Σ5 (210) GB, respectively, the cohesive energy increases to 4.3 and 4 J m^{-2}. We then investigated the effects of Zn additions to the GBs and found that the W_{sep} decreases almost linearly for both GBs, albeit with a steeper slope for the Σ5 (310) GB. For the case when no B is present at the GBs, four Zn atoms (=2 MLs) lower the work of separation to 2.3 J m^{-2} for the Σ5 (310) GB. The reduction of W_{sep} is less pronounced for the Σ5 (210) GB with 2 ML Zn to 3 J m^{-2}. If both B and Zn are considered, it is found that the cohesion reducing effects of Zn are compensated by the presence of B. Even when 3 Zn atoms (=1.5 ML) are added to both GBs, the work of separation is still higher than that of the pure interfaces. This shows that the effect of impurity atoms on GB cohesion is to a large extent purely additive.

From these observations clear implications can be established for GB-based alloy design to prevent LMIE. The addition of B and other impurity elements can reduce the tendency for Zn segregation, while the presence of cohesion enhancing elements such as B counteracts the embrittling tendency of Zn.

3. Discussion

In this study, the nanoscale segregation behavior of Zn in the presence of B and C at a Σ5 (310)[001] bcc-Fe tilt GB was investigated. It is found that Zn is forming a periodic, line-type segregation pattern with nanometer periodicity in regions with ≈5 at.% Zn bulk concentration. Despite the low Zn bulk concentration, strong modulation of Zn-rich (≈35 at.%) and Zn-lean (≈15 at.%) regions along the GB were observed which originate from a phase separation of the GB during cooling from the segregation transition at ≈403 °C according to our thermodynamically informed phase-field simulations. However, we can also not exclude the role of GB defects in the formation of this Zn segregation pattern. These Zn modulations alone would lead to local fluctuations in the work of separation along the GB, given the results obtained by DFT. Such local compositional variations at GBs have not been taken into account to explain the origins of LMIE or GB fracture.[3,4,6–9,35] From APT it is observed that the impurity elements B and C are homogeneously distributed within the GB plane in the same regions. However, their peak concentration is reduced compared to the as-grown bicrystal.[24] The asymmetric segregation profiles of B and C indicate that the GB has migrated during the annealing treatment either induced by Zn segregation[2,36] or through the triple line, where the GB is connected to the liquid Zn reservoir.[37] Our experimental observation of the GB structure show locally asymmetric segments with (430)/(410) and (010)/(110) facets. However, their structure is primarily composed of the symmetric Σ5 (310) as well as Σ5 (310) kite-type structural units of the GBs. This agrees with the work of Tschopp et al.,[38] who found that asymmetric boundaries can be built up by structural units from the delimiting symmetric GB structures when changing the GB habit plane orientation. Therefore, our first principles DFT calculations were performed for Σ5 (310) as well as Σ5 (210) symmetric GBs. The DFT calculations showed strong repulsive interactions between B and Zn as well as C and Zn. This negative interaction energy would lead to a significant reduction in the segregation tendency of Zn and ultimately leads to a reduction in the maximum Zn concentration at the GB, which by itself has a positive effect on GB cohesion. It should be mentioned that GB defects will generally increase the GB energy and, therefore, it can be expected that the segregation energy of defected boundaries is generally more negative compared to the ideal boundary. This is due to the correlation between GB energy and segregation energy. Higher GB energies lead to stronger segregation. Therefore, cohesion enhancing effects of solutes will generally be enhanced for defected boundaries (and embrittlement tendencies decreased). This follows from the Rice–Wang criterion.[39] However, further experiments are required to investigate the role of GB defects on solute segregation and GB cohesion. It should be noted that B and C were present at the boundary before Zn segregation. This is confirmed by our previous

investigations of a Zn-free bicrystal,[24] where B and C enriched the GB and depleted Al. With the introduction of Zn to the GB, a decrease of B and C at the GB core was observed. Whether this is related to the diffusion of Zn or the migration of the GB at the GB can not be fully resolved. Nevertheless, the calculations of the work of separation show that even lower levels of B or C comparable to those observed experimentally are capable to compensate the embrittling effects of Zn. Since both B and C are known to enhance GB cohesion,[24–28] our calculated values for the work of separation only considering B are a lower bound and it is shown in Figure S7 (Supporting Information) that C has a similarly positive effect on GB cohesion. To explore the impact of B and Zn on mechanical behavior of the GB, it would be necessary to perform nanomechanical tests below the brittle-to-ductile transition temperature from Region 1 and region 2, which will be performed in a separate study.

While LMIE is a complex, hierarchical process leading to material failure by the ingress of liquid metal along GBs, we focused our investigations on regions, where no intermetallic compounds formed but segregation of Zn as well as B and C occured. It has been indicated that GB composition and local cosegregation effects ahead of the crack tip are decisive in the underlying mechanisms.[7,14] Our work emphasizes the role of cohesion enhancing interstitials and how they can be used to prevent the segregation of detrimental solute elements which have the potential to reduce the cohesion strength of the GB. We demonstrate that segregation of interstitial elements can mitigate the embrittling effects of Zn by hindering its segregation to GBs and leveling its reduction in GB cohesion. Since it was recently shown that general GBs are composed of distinct structural units[40] and periodic segregation patterns can emerge at them,[41] our results can be qualitatively transferred to general GBs. However, further advancements in atomic-resolution experimentation and simulation methods are needed to fully describe such complex segregation behavior at random GBs with atomic precision. This work opens the path toward a promising route for materials design in which the controlled addition of B and C can act as an efficient agent for reducing Zn-mediated LMIE in steels.

4. Experimental Section

Experiment: For the experiments, a Fe-4at.% Al bicrystal with a global Σ5 [001] (310) was grown with the in-house Bridgman technique. The bulk concentration of B and C was determined by the purity of Fe-4at.% Al raw material used to grow the bicrystal. Wet chemical analysis of a 2 mm slice of the bicrystal showed a concentration of 0.001 at.% B and 0.05 at.% C. The bicrystal was cut into a ≈15 × 11 × 1 mm rectangle with the GB in the center. The steps how the bicrystal was coated with Zn are shown Figure S1 (Supporting Information). First, the sample was mechanically grinded and then chemically polished using a solution of 6% HF, 14% H_2O, and 80% H_2O_2. In order to prevent the contamination of the sample after polishing, the sample was held with steel rods. Afterward, the sample was immersed into a 99.999% Zn bath for 300 s. The temperature of the Zn bath was kept at 467 °C. The Zn was then ground off the large (001) surfaces as well as the large sides of the sample. Finally, the sample was encapsulated in a quartz tubes under vacuum (≈10^{-3} to 10^{-4} mbar) and annealed at 800 °C for 80 h. The Zn diffused bicrystal was mechanically polished until reaching a mirror-like surface. Microstructural characterization of the GB was done by EBSD (see Figure S2a, Supporting Information) as well as EDS, which were simultaneously carried out by means of a ThermoFisher Scios 2 dual beam FIB/SEM equipped with an EDAX Velocity EBSD camera and an EDAX Octane Elite Super EDS detector. From the characterized area, TEM plane-view specimens were prepared from two different regions using the Scios 2 FIB. STEM imaging as well as STEM–EDS were performed on a C_s probe-corrected FEI Titan Themis 60-300 kV operated at 300 kV as well as 120 kV equipped with the SuperX EDS detector system. The investigations were done with a semiconvergence angle of 17 mrad, a camera length of 100 mm and a probe current of 80 pA. The high resolution images were processed with a Butterworth filter and a Gaussian filter. The APT experiments were done in a CAMECA LEAP 5000 XS operated in laser-mode.

Computational Details–Atomistic Simulations: The computational details are described in more detail in refs. [24,42] but encompass first-principles density functional theory using the Vienna Ab initio Simulation Package (VASP) with projector augmented wave-functions.[43–46] For the exchange-correlation part, the PBE functional[47,48] was employed. Other parameters include the k-point mesh set as close as possible to 40 k-points $Å^{-1}$ for all involved simulation cells, and the energy cutoff with 400 eV. The GBs for simulations are constructed from two symmetrically misoriented slabs that meet at the GB on one side and on the other side are separated by a vacuum layer of at least 8 Å. Ferromagnetic behavior of the Fe atoms was considered for the construction of all simulations. Segregation energies were computed using[49]

$$E^x_{\mathrm{seg},i} = \left(E^x_{\mathrm{gb},i} - E_{\mathrm{gb}}\right) - \left(E^x_{\mathrm{bulk}} - E_{\mathrm{bulk}}\right) + \delta_{i-s}E_{\mathrm{Fe}} \tag{1}$$

with E_{gb} being the total energy of a GB without solute x, while $E^x_{\mathrm{gb},i}$ denotes the total energy of the same cell but with the solute x at the GB site i. For the reference of the solute in the bulk, the difference was computed between a bulk cell of 128 atoms without solute x and with solute x, E_{bulk}, and E^x_{bulk}, respectively. For considering the change of interstitial B in the bulk to a substitutional site at the GB, $\delta_{i-s} = 1$ and E_{Fe} corresponds to the total energy of a single Fe atom in its bulk structure. Segregation energies were connected to the solute enrichment at GBs via the White–Coghlan segregation isotherm[34] extended to multiple solutes. [50]

The work of separation was computed by separating the GB at all possible GB planes by at least 8 Å and computing the difference of the total energies for separated and joined GB slabs in the simulation cell.[9,42] The lowest obtained work of separation for each segregated state is considered as the most probable fracture plane.

Phase-Field Simulations: The composition- and temperature-dependent GB phase behavior as well as GB segregation evolution were explored using the thermodynamically informed phase-field modeling. The derivation and computational details of the model can be found in.[51] The CALPHAD integrated density-based free energy functional of the Fe–Zn system reads

$$\begin{aligned} G(\rho, X_{\mathrm{Zn}}, T) &= X_{\mathrm{Fe}}G_{\mathrm{Fe}}(\rho, T) + X_{\mathrm{Zn}}G_{\mathrm{Zn}}(\rho, T) \\ &+ \rho^2 \Delta H^{\mathrm{B}}_{\mathrm{mix}}(X_{\mathrm{Zn}}, T) - T\Delta S^{\mathrm{B}}_{\mathrm{mix}}(G_{\mathrm{Zn}}, T) \\ &+ \frac{\kappa_{X_{\mathrm{Zn}}}}{2}(\nabla X_{\mathrm{Zn}})^2 \end{aligned} \tag{2}$$

with $G_i(\rho, T) = \rho^2 E^{\mathrm{B}}_i + \rho(G^{\mathrm{B}}_i(T) - E^{\mathrm{B}}_i) + \frac{\kappa^\rho_i}{2}(\nabla\rho)^2$ and the atomic density $\rho \in [\rho^{\mathrm{GB}}, 1]$ ($\rho = 1$ for the bulk and $\rho = \rho^{\mathrm{GB}}$ at the GB plane). Here, the superscript B indicates bulk properties extracted from TCFE11 Thermo-Calc database: G^{B}_i was the free energy, E^{B}_i the potential energy and $\Delta H^{\mathrm{B}}_{\mathrm{mix}}$ and $\Delta S^{\mathrm{B}}_{\mathrm{mix}}$ were the mixing enthalpy and entropy, respectively. The gradient energy coefficients κ^ρ_i and $\kappa_{X_{\mathrm{Zn}}}$ accounts for the structural and chemical heterogeneity with the GB region.

In order to understand the GB phase behavior the GB phase diagram must be investigated. The GB miscibility gap was calculated for $\rho^{\mathrm{GB}} = 0.92$ which corresponds to the current Σ5 [001] GBs. Figure S9, Supporting Information, shows the density profiles across the GBs computed from previous atomistic simulations.[52] The bulk and GB miscibility gaps were computed using a robust implementation of the common tangent construction and verified versus Thermo-Calc calculations: For this purpose,

first the chemical potential $\frac{\partial G}{\partial X_{Zn}}$ was calculated from the Gibbs free energy, Equation (2), for $\rho = 0.92$. Subsequently, at any given temperature, the common tangent was calculated, through the Maxwell construction, to obtain the GB miscibility gap. To investigate GB segregation, the equal chemical potential condition was applied, that is, the equilibrium GB composition was the one composition that gives the same chemical potential as the corresponding bulk. Computing the critical alloy compositions and temperatures at which a low- to high-segregation transition takes place was of special interest. This was one key result presented in Figure 5a. To study the GB decomposition behavior, 3D density-based phase-field simulations were performed using an Openmp parallel C++ code with adaptive time-stepping. The simulation domain has been $17 \times 17 \times 3.4$ nm^3 with $dx = 0.17$ nm. Further details of simulation methods can be found in refs. [53,54].

Supporting Information

Supporting Information is available from the Wiley Online Library or from the author.

Acknowledgements

The authors gratefully acknowledge the financial support under the scope of the COMET program within the K2 Center "Integrated Computational Material, Process and Product Engineering (IC-MPPE)" (project no. 886385). This program was supported by the Austrian Federal Ministries for Climate Action, Environment, Energy, Mobility, Innovation and Technology (BMK) and for Digital and Economic Affairs (BMDW), represented by the Austrian Research Promotion Agency (FFG), and the federal states of Styria, Upper Austria and Tyrol. X.Z. was supported by the Alexander-Humboldt-Stiftung. R.D.K. gratefully acknowledges support from German Research Foundation (DFG) through projects DA 1655/2-1 and DA 1655/3-1. G.D. gratefully acknowledges support by the ERC Advanced Grant GB-Correlate (grant agreement 787446).

Open access funding enabled and organized by Projekt DEAL.

Conflict of Interest

The authors declare no conflict of interest.

Author Contributions

G.D., W.E., and L.R. secured funding. C.H.L. and A.A. designed the experiments. C.H.L. supervised the project and A.A. conducted the electron microscopy experiments including STEM and FIB/SEM. X.Z. conducted the APT experiments. D.S. performed the atomistic simulations. R.D.K. executed the thermodynamic and phase-field simulations. C.H.L., L.R., and B.G. contributed to the data analysis. A.A., D.S., and C.H.L. wrote the paper. X.Z., B.G., R.K.D., W.E., L.R., and G.D. revised the paper.

Data Availability Statement

The data and code that support the findings of this study are available from the corresponding author upon reasonable request.

Keywords

grain boundary embrittlement, grain boundary segregation, liquid metals, nanoscale segregation patterns, zinc

Received: December 16, 2022
Revised: March 17, 2023
Published online:

[1] P. Lejček, M. Šob, *J. Mater. Sci.* **2014**, *49*, 2477.
[2] M. Hillert, G. R. Purdy, *Acta Metall.* **1978**, *26*, 333.
[3] C. Beal, X. Kleber, D. Fabregue, M. Bouzekri, *Scr. Mater.* **2012**, *66*, 1030.
[4] L. Cho, H. Kang, C. Lee, B. C. De Cooman, *Scr. Mater.* **2014**, *90–91*, 25.
[5] R. Ashiri, M. A. Haque, C.-W. Ji, M. Shamanian, H. R. Salimijazi, Y.-D. Park, *Scr. Mater.* **2015**, *109*, 6.
[6] M. H. Razmpoosh, A. Macwan, E. Biro, D. L. Chen, Y. Peng, F. Goodwin, Y. Zhou, *Mater. Des.* **2018**, *155*, 375.
[7] M. H. Razmpoosh, A. Macwan, F. Goodwin, E. Biro, Y. Zhou, *Metall. Mater. Trans. A* **2020**, *51*, 3938.
[8] Y. Ikeda, R. Yuan, A. Chakraborty, H. Ghassemi-Armaki, J. Zuo, R. Maaß, *Mater. Today Adv.* **2022**, *13*, 100196.
[9] D. Scheiber, K. Prabitz, L. Romaner, W. Ecker, *Acta Mater.* **2020**, *195*, 750.
[10] P. J. L. Fernandes, D. R. H. Jones, *Int. Mater. Rev.* **1997**, *42*, 251.
[11] N. S. Stoloff, T. L. Johnston, *Acta Metall.* **1963**, *11*, 251.
[12] A. R. C. Westwood, M. H. Kamdar, *Philos. Mag. A* **1963**, *8*, 787.
[13] P. Gordon, H. H. An, *Metal. Mater. Trans. A* **1982**, *13*, 457.
[14] C. DiGiovanni, A. Ghatei Kalashami, E. Biro, N. Y. Zhou, *Materialia* **2021**, *18*, 101153.
[15] R. Schweinfest, A. T. Paxton, M. W. Finnis, *Nature* **2004**, *432*, 1008.
[16] E. Senel, J. C. Walmsley, S. Diplas, K. Nisancioglu, *Corros. Sci.* **2014**, *85*, 167.
[17] M. Yuasa, M. Mabuchi, *Phys. Rev. B* **2010**, *82*, 094108.
[18] R. Wu, A. J. Freeman, G. B. Olson, *Science* **1994**, *265*, 376.
[19] R. Wu, A. J. Freeman, G. B. Olson, *Phys. Rev. B* **1994**, *50*, 75.
[20] W. Peng, H. Peng, G. Wu, J. Zhang, *Comput. Mater. Sci.* **2020**, *171*, 109204.
[21] W. T. Geng, A. J. Freeman, G. B. Olson, *Phys. Rev. B* **2001**, *63*, 165415.
[22] M. Razmpoosh, C. DiGiovanni, Y. Zhou, E. Biro, *Prog. Mater Sci.* **2021**, *121*, 100798.
[23] D. Bhattacharya, L. Cho, E. van der Aa, A. Pichler, N. Pottore, H. Ghassemi-Armaki, K. O. Findley, J. G. Speer, *Mater. Sci. Eng. A* **2021**, *804*, 140391.
[24] A. Ahmadian, D. Scheiber, X. Zhou, B. Gault, C. H. Liebscher, L. Romaner, G. Dehm, *Nat Commun.* **2021**, *12*, 6008.
[25] R. Wu, A. J. Freeman, G. B. Olson, *Phys. Rev. B 53*, 7504.
[26] A. Fraczkiewicz, *Mater. Trans. JIM* **2000**, *41*, 166.
[27] J. Wang, R. Janisch, G. K. H. Madsen, R. Drautz, *Acta Mater.* **2016**, *115*, 259.
[28] N. Miyazawa, M. Hakamada, M. Mabuchi, *Philos. Mag. Lett. 97*, 311.
[29] A. S. Kholtobina, W. Ecker, R. Pippan, V. I. Razumovskiy, *Comput. Mater. Sci.* **2021**, *188*, 110215.
[30] D. H. R. Fors, G. Wahnström, *Phys. Rev. B* **2008**, *77*, 132102.
[31] P. J. Felfer, B. Gault, G. Sha, L. Stephenson, S. P. Ringer, J. M. Cairney, *Microsc. Microanal.* **2012**, *18*, 359.
[32] A. Kwiatkowski da Silva, R. Darvishi Kamachali, D. Ponge, B. Gault, J. Neugebauer, D. Raabe, *Acta Mater. 168*, 109.
[33] X. Su, N.-Y. Tang, J. M. Toguri, *J. Alloys Compd.* **2001**, *325*, 129.
[34] C. L. White, W. A. Coghlan, *Metall. Mater. Trans. A* **1977**, *8*, 1403.
[35] R. Ashiri, M. Shamanian, H. R. Salimijazi, M. A. Haque, J.-H. Bae, C.-W. Ji, K.-G. Chin, Y.-D. Park, *Scr. Mater.* **2016**, *114*, 41.
[36] E. Rabkin, B. B. Straumal, V. G. Sursaeva, L. S. Shvindlerman, R. Fournelle, W. Gust, *Mater. Sci. Forum* **1993**, *126–128*, 321.
[37] J. S. Dohie, J. Cahoon, W. Caley, *JPED* **2007**, *28*, 322.
[38] M. A. Tschopp, D. L. Mcdowell, *Philos. Mag.* **2007**, *87*, 3871.
[39] J. R. Rice, J.-S. Wang, *Mater. Sci. Eng. A* **1989**, *107*, 23.
[40] C. Wang, H. Duan, C. Chen, P. Wu, D. Qi, H. Ye, H.-J. Jin, H. L. Xin, K. Du, *Matter* **2020**, *3*, 1999.

[41] Z. Yu, P. R. Cantwell, Q. Gao, D. Yin, Y. Zhang, N. Zhou, G. S. Rohrer, M. Widom, J. Luo, M. P. Harmer, *Science* **2017**, *358*, 97.
[42] D. Scheiber, L. Romaner, R. Pippan, P. Puschnig, *Phys. Rev. Mater.* **2018**, *2*, 093609.
[43] G. Kresse, J. Hafner, *Phys. Rev. B* **1993**, *47*, 558.
[44] G. Kresse, J. Furthmüller, *Comput. Mater. Sci.* **1996**, *6*, 15.
[45] G. Kresse, J. Furthmüller, *Phys. Rev. B* **1996**, *54*, 11169.
[46] G. Kresse, D. Joubert, *Phys. Rev. B* **1999**, *59*, 1758.
[47] J. P. Perdew, K. Burke, M. Ernzerhof, *Phys. Rev. Lett.* **1996**, *77*, 3865.
[48] J. Perdew, K. Burke, M. Ernzerhof, *Phys. Rev. Lett.* **1998**, *80*, 891.
[49] A. S. Ebner, S. Jakob, H. Clemens, R. Pippan, V. Maier-Kiener, S. He, W. Ecker, D. Scheiber, V. I. Razumovskiy, *Acta Mater.* **2021**, *221*, 117354.
[50] D. Scheiber, T. Jechtl, J. Svoboda, F. Fischer, L. Romaner, *Acta Mater.* **2020**, *182*, 100.
[51] R. D. Kamachali, *RSC Adv.* **2020**, *10*, 26728.
[52] S. Ratanaphan, D. L. Olmsted, V. V. Bulatov, E. A. Holm, A. D. Rollett, G. S. Rohrer, *Acta. Mater.* **2015**, *88*, 346.
[53] R. Darvishi Kamachali, A. Kwiatkowski da Silva, E. McEniry, D. Ponge, B. Gault, J. Neugebauer, D. Raabe, *npj Comput. Mater.* **2020**, *6*, 191.
[54] T. Wallis, R. D. Kamachali, *Acta Mater.* **2023**, *242*, 118446.